Electrical Tuning of Ferromagnetic Resonance in Thin-Film Nanomagnets Coupled to Piezoelectrically Active Substrates

A. V. Azovtsev and N. A. Pertsev[*]

Ioffe Institute, 194021 St. Petersburg, Russia

Electrical manipulation and control of magnetic nanostructures could greatly reduce the power consumption of spintronic devices. We theoretically describe the strain-mediated electric-field control of ferromagnetic resonance (FMR) in thin-film nanomagnets integrated onto active substrates experiencing voltage-induced piezoelectric deformations. To that end, we first consider the general problem of FMR in ferromagnetic films and islands with nanoscale thicknesses mechanically coupled to much thicker passive or active substrates. An analytic relation is derived for the resonance frequency of such nanomagnets, which takes into account the influence of both substrate-induced lattice strains and surface/interface magnetic anisotropy. This general relation is valid for any equilibrium orientation of the magnetization and renders possible to calculate the FMR frequency and resonance magnetic field with the account of strain-driven and size-induced spin reorientation transitions (SRTs). Next, we quantitatively describe the electrical tuning of FMR frequency in ultrathin Ni, Fe, and $Fe_{60}Co_{40}$ layers coupled to various piezoelectrically active substrates, including conventional and relaxor ferroelectrics. The results of numerical calculations are presented in the form of resonance frequency and electrical tunability maps, where the thickness of the ferromagnetic layer and the electric field applied to the substrate are used as two parameters. It is shown that the FMR frequency strongly decreases near the SRT lines on the thickness–field plane, whereas the tunability increases drastically at most SRTs driven by substrate-induced lattice strains. This remarkable feature provides an efficient electric-field control of FMR, which is necessary for the development of signal processing microwave devices with high tuning speed and low energy consumption.

I. INTRODUCTION

The precessional motion of the magnetization vector plays an important role in the dynamics of ferromagnets, arising in the course of magnetization relaxation to an equilibrium orientation, precessional magnetic switching, and magnetization oscillations near the equilibrium direction induced by a cyclic stimulus. The amplitude of magnetization precession driven by a microwave magnetic field increases drastically near the resonance frequency, which constitutes the phenomenon of ferromagnetic resonance (FMR). Experimental studies of the FMR provided fundamental information on the physical characteristics of ferromagnetic crystals, thin films, and heterostructures, including the magnetic anisotropy, interlayer exchange coupling, and damping of magnetization precession [1–3]. Moreover, FMR is employed in a variety of signal processing rf/microwave devices, such as phase shifters, tunable band-stop filters, resonators, and signal-to-noise enhancers [4–7].

The magnetic dynamics occurring at a temperature well below the Curie point T_c can be described by

the Landau-Lifshitz-Gilbert (LLG) torque equation of motion for the time-dependent magnetization $\mathbf{M}(t)$ [3]. This equation involves a torque $\mathbf{T}_{eff} = \mathbf{M} \times \mathbf{H}_{eff}$ created by the effective magnetic field $\mathbf{H}_{eff}$ defined by the relation $\mu_0 \mathbf{H}_{eff} = -\partial F / \partial \mathbf{M}$, where μ_0 is the vacuum permeability and F is the Helmholtz free energy density of a ferromagnet. The precession of the vector $\mathbf{M}(t) = \mathbf{M}_s + \delta \mathbf{M}(t)$ around the static magnetization $\mathbf{M}_s$ is usually excited by a microwave magnetic field $\mathbf{h}(t)$ orthogonal to $\mathbf{M}_s$ [3]. However, any stimulus creating nonzero torque $\mathbf{T}_{eff}(t)$ by means of a periodic modulation of the energy density F could be used to generate the magnetization precession as well. For example, in ferromagnets exhibiting significant magnetostriction, magnetization oscillations can be induced by elastic waves [8–10]. Furthermore, an electrically driven magnetization precession in ferromagnetic nanostructures with voltage-controlled interfacial magnetic anisotropy was observed and explained theoretically [11–14]. Interestingly, the FMR can be created even by a spin-polarized current flowing in a conductive nanostructure, because such a current exerts a spin-transfer torque on the magnetization, which should be added to the LLG equation [15–17].

---

[*]pertsev.domain@mail.ioffe.ru

The tuning of FMR frequency is usually achieved with the aid of a dc magnetic field [3], but this approach suffers from slow tuning speed and high energy consumption [18]. On the other hand, the LLG equation suggests that resonance conditions can be controlled via the magnetoelastic coupling between spins and static lattice strains [3,18–21]. This feature renders possible to tune the FMR by a dc voltage applied to a piezoelectric material mechanically coupled to a ferromagnetic one in a hybrid material system. As expected from theoretical considerations, electrically induced shifts of the FMR frequency and field were observed in ferrite-piezoelectric composites and ferromagnetic films deposited on ferroelectric substrates [18,20,22–25]. The experimental and theoretical studies demonstrated that ferromagnetic-piezoelectric hybrids are promising for the development of next-generation rf/microwave devices and communication systems [18,24].

In this paper, we theoretically study the FMR in thin-film nanomagnets – ferromagnetic films and islands with nanoscale thicknesses, which are coupled to piezoelectrically active substrates (Fig. 1). First, the FMR frequency is calculated as a function of substrate-induced lattice strains for (001)-oriented ultrathin epitaxial layers of cubic ferromagnets with the account of the surface/interface magnetic anisotropy. To this end, general analytic relations are derived for the energy derivatives involved in the Smit-Beljers formula, which makes it possible to determine the resonance frequency and field for any equilibrium direction of the magnetization. Second, the tuning of FMR frequency by a voltage applied to a piezoelectrically active substrate is described with the account of spin reorientation transitions (SRTs) occurring in ultrathin ferromagnetic layers. Numerical calculations of the resonance frequency and its electrical tunability are performed for Ni, Fe, and $Fe_{60}Co_{40}$ films coupled to various piezoelectric materials – simple piezoelectric crystals, conventional ferroelectrics, and relaxor ferroelectrics. It is shown that the tunability of the FMR frequency increases drastically at most SRTs driven by substrate-induced lattice strains.

II. STRAIN AND SURFACE/INTERFACE EFFECTS ON FMR IN FERROMAGNETIC FILMS

We first consider the general problem of FMR in a ferromagnetic (FM) film or island mechanically coupled to a much thicker homogeneous passive or active substrate. At such geometry, the film appears to be under mixed mechanical boundary conditions, which involve fixed in-plane strains u_1, u_2, u_6 controlled by the substrate and zero stresses σ_3, σ_4, σ_5 at the film free surface [26]. (We use the Voigt matrix notation and a Cartesian reference frame with the x_3 axis orthogonal to the film plane.)
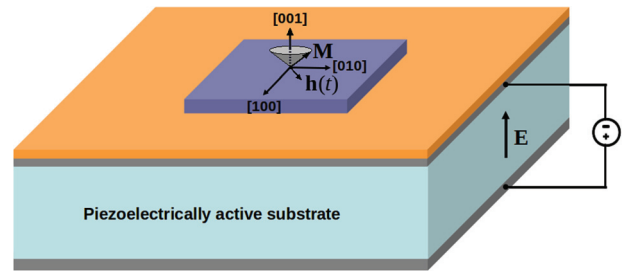

FIG. 1.   Ultrathin ferromagnetic film mechanically coupled to a piezoelectrically active substrate. A microwave magnetic field $\mathbf{h}(t)$ induces precession of the magnetization vector $\mathbf{M}$ around the equilibrium direction. The resonance frequency of the magnetization precession can be tuned by an electric field $\mathbf{E}$ created in the substrate sandwiched between the top and bottom electrodes connected to a voltage source. Such electrical tuning is provided by the substrate piezoelectric deformations that modify lattice strains in the film.

In the case of a single-crystalline FM film with a thickness t_f smaller than the exchange length and nanoscale in-plane dimensions L_1, $L_2 \gg t_f$, spatial distributions of the magnetization $\mathbf{M}$ and lattice strains $\mathbf{u}$ may be assumed uniform. Indeed, although the magnetoelastic coupling could lead to a nonhomogeneous magnetic ground state under certain circumstances [27–29], a single-domain state is expected to form in nanolayers with in-plane dimensions, which do not strongly exceed the width w of FM domain walls. Since domain walls in the considered ferromagnets have thicknesses about 50–100 nm [30], the upper limit of L_1, $L_2 \le w$ should be of the order of 100 nm. Furthermore, at L_1, $L_2 \gg t_f$ the edge effects may be neglected, and the magnetic state of the FM nanolayer can be defined by the direction cosines m_i ($i = 1,2,3$) of the unit vector $\mathbf{m} = \mathbf{M}/M_s$, because the magnetization magnitude $|\mathbf{M}| = M_s$ at a given temperature $T \ll T_c$ can be regarded as a fixed quantity.

To describe the energetics of a homogeneously magnetized ultrathin film, we employ the effective volumetric energy density $F(t_f)$ given by the sum of the bulklike contribution independent of the film thickness t_f and the total specific energy of two film surfaces divided by t_f [26,31]. At temperatures $T \ll T_c$, both contributions to F can be described by polynomials in terms of the direction cosines m_i defined in the crystallographic reference frame of the prototypic paramagnetic phase [3]. For our purposes, it is necessary to take into account the influence of substrate-induced lattice strains [21,26] and to allow for both the second-order and fourth-order terms in the series expansion of the surface/interface magnetic anisotropy [32,33]. A suitable polynomial has recently been reported for (001)-oriented epitaxial films of cubic ferromagnets [34]. Adding to this polynomial the Zeeman energy accounting for the influence of external magnetic field $\mathbf{H}$, we obtain the magnetization-dependent part $\Delta F(m_i)$ of the energy

density in the form

$$\Delta F = \left(K_{1||} + \frac{K_{s||}}{t_f}\right) m_1^2 m_2^2 + \left(K_{1\perp} + \frac{K_{s\perp}}{t_f}\right)$$

$$(m_1^2 + m_2^2)m_3^2 + K_2 m_1^2 m_2^2 m_3^2 + B_1(u_1 m_1^2 + u_2 m_2^2)$$

$$+ B_2 u_6 m_1 m_2 - B_1 \left[\frac{B_1}{6c_{11}} + \frac{c_{12}}{c_{11}}(u_1 + u_2)\right] m_3^2$$

$$+ \frac{K_s}{t_f} m_3^2 + \frac{1}{2}\mu_0 M_s^2 (N_{11}m_1^2 + 2N_{12}m_1 m_2 + N_{22}m_2^2$$

$$+ N_{33}m_3^2) - \mu_0 M_s(H_1 m_1 + H_2 m_2 + H_3 m_3), \quad (1)$$

where $K_{1||}$, $K_{1\perp}$, and K_2 are the coefficients of the fourth- and sixth-order terms defining the bulklike magnetocrystalline anisotropy at fixed strains $\mathbf{u}$, K_s, $K_{s||}$, $K_{s\perp}$ are the coefficients of the second- and fourth-order terms in the polynomial expansion of the surface or interfacial magnetic anisotropy, B_1, B_2 are the magnetoelastic coupling constants [35], c_{11}, c_{12} are the elastic stiffnesses at fixed magnetization, and N_{ij} are the demagnetizing factors (N_{13} and N_{23} can be set to zero for films with in-plane dimensions L_1, $L_2 \gg t_f$). The presence of a strain-induced contribution to the surface/interface magnetic anisotropy can be taken into account by introducing thickness-dependent magnetoelastic coefficients B_1 and B_2, which may be written as $B_1 = B_1^b + B_1^s/t_f$ and $B_2 = B_2^b + B_2^s/t_f$ [36].

The differentiation of Eq. (1) with respect to m_i yields the components $H_i^{\text{eff}} = -(\mu_0 M_s)^{-1}\partial F/\partial m_i$ of the effective field acting on the magnetization. The equilibrium magnetization orientation in the absence of the microwave field $\mathbf{h}(t)$ can be found either using the equation $\mathbf{M} \times \mathbf{H}_{\text{eff}} = 0$ or by direct numerical minimization of the energy density ΔF under the condition $m_1^2 + m_2^2 + m_3^2 = 1$. Such a procedure implies determination of all local minima of ΔF and selection of the orientation that corresponds to minimum minimorum.

Equation (1) shows that the effect of lattice strains u_1, u_2, u_6, which should be measured from the prototypic cubic phase with $\mathbf{M} = 0$, is mathematically equivalent to the renormalization of the film's demagnetizing factors N_{ij}. Introducing the effective anisotropy constants $K_{||} = K_{1||} + K_{s||}/t_f$, $K_{\perp} = K_{1\perp} + K_{s\perp}/t_f$ and the effective demagnetizing factors $N_{11}^* = N_{11} + 2B_1 u_1/(\mu_0 M_s^2)$, $N_{12}^* = N_{12} + B_2 u_6/(\mu_0 M_s^2)$, $N_{22}^* = N_{22} + 2B_1 u_2/(\mu_0 M_s^2)$, $N_{33}^* = N_{33} - 2B_1[(B_1/6c_{11}) + (c_{12}/c_{11})(u_1 + u_2)]/(\mu_0 M_s^2) + 2K_s/(\mu_0 M_s^2 t_f)$ taking into account both the strain and surface effects, we cast Eq. (1) into a compact form

$$\Delta F = K_{||}m_1^2 m_2^2 + K_{\perp}(m_1^2 + m_2^2)m_3^2 + K_2 m_1^2 m_2^2 m_3^2$$

$$+ \frac{1}{2}\mu_0 M_s^2(N_{11}^* m_1^2 + 2N_{12}^* m_1 m_2 + N_{22}^* m_2^2 + N_{33}^* m_3^2)$$

$$- \mu_0 M_s(H_1 m_1 + H_2 m_2 + H_3 m_3). \quad (2)$$

Next, using the relations $m_1 = \cos\varphi \sin\theta$, $m_2 = \sin\varphi \sin\theta$, and $m_3 = \cos\theta$, one can write the energy density ΔF as a function of the polar angle θ and the azimuth angle φ defining the magnetization direction in the spherical coordinate system. Then the FMR frequency ν_{res} can be calculated via the Smit-Beljers formula $\nu_{\text{res}} = \gamma\sqrt{\Delta F_{\theta\theta}\Delta F_{\varphi\varphi} - \Delta F_{\theta\varphi}^2}/(2\pi M_s \sin\theta)$, where γ is the electron's gyromagnetic ratio, and the quantities under the square root are the second derivatives of ΔF with respect to the angles θ and φ [3]. It should be emphasized that this formula implies the substitution of equilibrium orientation angles, which satisfy the system of equations $\partial\Delta F/\partial\phi = 0$, $\partial\Delta F/\partial\theta = 0$, and well-known inequalities imposed on the second derivatives of ΔF. In addition, it ignores the effect of damping on the FMR frequency; however, estimates using the available analytical relation allowing for the Gilbert damping [13] show that this effect is usually negligible.

Differentiating Eq. (2), we derive explicit expressions for the second derivatives of ΔF involved in the Smit-Beljers formula. Using the equilibrium conditions to get rid of the denominator in this formula, after some mathematical manipulation, we obtain the following general relations for the derivative $\Delta F_{\theta\theta}$ and the ratios $\Delta F_{\varphi\varphi}/\sin^2\theta$ and $\Delta F_{\theta\varphi}/\sin\theta$ governing the FMR frequency:

$$\Delta F_{\theta\theta} = \mu_0 M_s H[\cos(\varphi - \varphi_H)\sin\theta\sin\theta_H + \cos\theta\cos\theta_H]$$

$$+ \mu_0 M_s^2(N_{11}^*\cos^2\varphi + N_{12}^*\cos\varphi\sin\varphi$$

$$+ N_{22}^*\sin^2\varphi - N_{33}^*)\cos 2\theta + 2K_{\perp}\cos 4\theta$$

$$+ \frac{1}{2}K_{||}\sin^2 2\varphi(\cos 2\theta - \cos 4\theta)$$

$$+ \frac{1}{32}K_2\sin^2 2\varphi(\cos 2\theta + 8\cos 4\theta - 9\cos 6\theta),$$

$$\frac{\Delta F_{\varphi\varphi}}{\sin^2\theta} = \mu_0 M_s H[\cos(\varphi - \varphi_H)\sin\theta\sin\theta_H + \cos\theta\cos\theta_H]$$

$$+ \mu_0 M_s^2[N_{11}^*(\sin^2\varphi - \cos^2\varphi\sin^2\theta)$$

$$- N_{12}^*\cos\varphi\sin\varphi(1 + \sin^2\theta) + N_{22}^*(\cos^2\varphi$$

$$- \sin^2\varphi\sin^2\theta) - N_{33}^*\cos^2\theta] + 2K_{\perp}\cos 2\theta\cos^2\theta$$

$$+ K_{||}[2 - \sin^2 2\varphi(3 + \sin^2\theta)]\sin^2\theta$$

$$+ \frac{1}{8}K_2[4 - 3\sin^2 2\varphi(2 + \sin^2\theta)]\sin^2 2\theta,$$

$$\frac{\Delta F_{\theta\varphi}}{\sin\theta} = \frac{1}{2}\mu_0 M_s^2[(N_{22}^* - N_{11}^*)\sin 2\varphi + N_{12}^*\cos 2\varphi]\cos\theta$$

$$+ \frac{3}{2}K_{||}\sin 4\varphi\cos\theta\sin^2\theta$$

$$+ \frac{1}{4}K_2\sin 4\varphi\sin\theta\sin 2\theta(3 - 5\sin^2\theta), \quad (3)$$

where φ_H, θ_H are the angles defining the direction of the static magnetic field **H** in the spherical coordinate system. Importantly, Eq. (3) makes it possible to calculate the resonance frequency for any equilibrium orientation of the magnetization **M**, being valid even at $\theta = 0$. In the particular case of $\theta = \theta_H = 0$, the calculation yields

$$
\left(\frac{2\pi \nu_{\text{res}}}{\gamma}\right)^2 = \mu_0^2[H^2 + HM_s(N_{11}^* + N_{22}^* - 2N_{33}^*)
$$
$$
+ M_s^2(N_{11}^* N_{22}^* - \frac{1}{4}N_{12}^{*2} - N_{11}^* N_{33}^* - N_{22}^* N_{33}^*
$$
$$
+ N_{33}^{*2})] + 2\mu_0[2H + M_s(N_{11}^*
$$
$$
+ N_{22}^* - 2N_{33}^*)]\frac{K_\perp}{M_s} + 4\frac{K_\perp^2}{M_s^2}. \tag{4}
$$

The dependence of ν_{res} on the angle θ at $\varphi = \varphi_H = 0$ (requiring $N_{12}^* = 0$) is defined by the relation

$$
\left(\frac{2\pi \nu_{\text{res}}}{\gamma}\right)^2 = [\mu_0 H \cos(\theta - \theta_H) + \mu_0 M_s
$$
$$
\times (N_{11}^* - N_{33}^*) \cos 2\theta + \frac{2K_\perp}{M_s}\cos 4\theta]
$$
$$
[\mu_0 H \cos(\theta - \theta_H) - \mu_0 M_s
$$
$$
\times (N_{11}^* \sin^2\theta - N_{22}^* + N_{33}^* \cos^2\theta)
$$
$$
+ \frac{2K_\perp}{M_s}\cos 2\theta\cos^2\theta + \frac{2K_\parallel}{M_s}\sin^2\theta
$$
$$
+ \frac{K_2}{2M_s}\sin^2 2\theta], \tag{5}
$$

while at $\varphi = \varphi_H = 45°$ (requiring $N_{11}^* = N_{22}^*$), this dependence takes the form

$$
\left(\frac{2\pi \nu_{\text{res}}}{\gamma}\right)^2 = [\mu_0 H \cos(\theta - \theta_H) + \frac{1}{2}\mu_0 M_s(2N_{11}^* + N_{12}^*
$$
$$
- 2N_{33}^*)\cos 2\theta + \frac{2K_\perp}{M_s}\cos 4\theta
$$
$$
+ \frac{K_\parallel}{2M_s}(\cos 2\theta - \cos 4\theta)
$$
$$
+ \frac{K_2}{32M_s}(\cos 2\theta + 8\cos 4\theta - 9\cos 6\theta)]
$$
$$
\times [\mu_0 H \cos(\theta - \theta_H)
$$
$$
+ \frac{1}{2}\mu_0 M_s(2N_{11}^* + N_{12}^* - 2N_{33}^*)\cos^2\theta
$$

$$
- \mu_0 M_s N_{12}^* + \frac{2K_\perp}{M_s}\cos 2\theta\cos^2\theta
$$
$$
- \frac{K_\parallel}{M_s}(2 - 3\cos^2\theta + \cos^4\theta)
$$
$$
- \frac{K_2}{2M_s}(5\cos^2\theta - 8\cos^4\theta + 3\cos^6\theta)]. \tag{6}
$$

For in-plane equilibrium magnetization orientations ($\theta = \theta_H = 90°$), the general relation for the FMR frequency reads

$$
\left(\frac{2\pi \nu_{\text{res}}}{\gamma}\right)^2 = \left[\mu_0 H \cos(\varphi - \varphi_H) - \mu_0 M_s(N_{11}^* \cos^2\varphi\right.
$$
$$
+ N_{12}^* \sin\varphi \cos\varphi + N_{22}^* \sin^2\varphi - N_{33}^*) + \frac{2K_\perp}{M_s}
$$
$$
\left. - \frac{2K_\parallel - K_2}{2M_s}\sin^2 2\varphi\right]\left\{\mu_0 H \cos(\varphi - \varphi_H)\right.
$$
$$
- \mu_0 M_s[(N_{11}^* - N_{22}^*)\cos 2\varphi + N_{12}^* \sin 2\varphi]
$$
$$
\left. + \frac{2K_\parallel}{M_s}\cos 4\varphi\right\}. \tag{7}
$$

At $N_{11}^* = N_{12}^* = N_{22}^* = 0$, $N_{33}^* = 1$, and $K_2 = 0$, Eqs. (4)–(7) reduce to formulas which agree with the previous results obtained for some particular magnetization orientations [3,33] provided that one allows for the difference between Eq. (1) and the expression used for the film energy density in Refs. [3,33]. The validity of our analytic calculations is confirmed by computer simulations performed in the macrospin approximation via the numerical solution of the LLG equation. It should be noted that the resonance magnetic field $\mathbf{H}_{\text{res}}(\nu)$ corresponding to a given frequency ν of the microwave excitation field $\mathbf{h} = \mathbf{h}_{\text{max}}\sin(2\pi\nu t)$ can be calculated using Eq. (3) as well. The derived analytical relations provide the basis for theoretical calculations of the strain and size effects on the resonance frequency and field of single-domain FM films and islands.

III. STRAIN-MEDIATED ELECTRIC-FIELD CONTROL OF FMR IN THIN-FILM NANOMAGNETS

In general, the substrate-induced strain **u** in a FM overlayer is the sum of initial misfit strain $\mathbf{u}_0$ and additional contribution $\delta\mathbf{u}$ created by an external electric or magnetic field applied to an "active" piezoelectric or magnetostrictive substrate [26,37]). The field-induced strains $\delta\mathbf{u}$ result from the substrate deformations and their transfer to the overlayer owing to the interfacial mechanical coupling. In the case of the piezoelectrically active substrates considered in this work, electrically generated substrate deformations may either linearly depend on the

TABLE I.　Material parameters of ferromagnetic films used in numerical calculations.

	Ni	Fe	$Fe_{60}Co_{40}$
M_s (A m^{-1})	4.2×10^5 [33]	1.7×10^6 [48]	1.8×10^6 [50]
$K_{1\parallel}$ (J m^{-3})	-1.44×10^5 [33]	10^5 [48]	-10^4 [51]
$K_{1\perp}$ (J m^{-3})	-7.26×10^4 [33]	10^5 [34,48]	-10^4 [51]
K_2 (J m^{-3})	-0.23×10^4 [41]	1.5×10^4 [41]	0 [34]
K_s (J m^{-2})	6×10^{-4} [40]	-9×10^{-4} [34,48]	-10^{-3} [52]
$K_{s\parallel}$ (J m^{-2})	1.98×10^{-4} [33]	-4.5×10^{-5} [34]	10^{-5} [51]
$K_{s\perp}$ (J m^{-2})	1.02×10^{-4} [33]	-4.5×10^{-5} [34,48]	10^{-5} [51]
B_1 (J m^{-3})	9.2×10^6 [41]	-3.3×10^6 [41]	-30×10^6 [49]
c_{11} (N m^{-2})	2.465×10^{11} [42]	2.42×10^{11} [42]	2.8×10^{11} [42]
c_{12} (N m^{-2})	1.473×10^{11} [42]	1.465×10^{11} [42]	1.4×10^{11} [42]

field intensity **E** or vary in a nonlinear and hysteretic manner, as happens in ferroelectric crystals experiencing phase transformations or ferroelastic domain switching [23,28,38,39]. For clarity, we restrict further analysis by linear variations of piezoelectric deformations and focus on the most advantageous hybrid structure, where the substrate is sandwiched between the top and bottom electrodes (Fig. 1). Accordingly, we may write in-plane film strains involved in the effective demagnetizing factors N_{ij}^* as $u_1 = u_1^0 + \xi_1 d_{31} E_3$, $u_2 = u_2^0 + \xi_2 d_{32} E_3$, and $u_6 = u_6^0 + \xi_6 d_{36} E_3$, where d_{in} are the substrate piezoelectric coefficients in the matrix notation defined in the film reference frame, and $\xi_n \leq 1$ are the strain transfer parameters depending on the quality of interfaces [34,39]. Calculating N_{ij}^* with the account of these relations and substituting them into Eqs. (2) and (3), one can determine dependences of the equilibrium magnetization orientation and the FMR frequency on the electric field E_3 created in the piezoelectric substrate.

To quantify the efficiency of strain-mediated electric-field control of FMR, we perform numerical calculations for (001)-oriented Ni, Fe, and $Fe_{60}Co_{40}$ films coupled to piezoelectric substrates not inducing in-plane shear strains in FM overlayers ($u_6^0 = 0$ and $d_{36} = 0$). Theoretical results are presented in the form of FMR maps, where the resonance frequency ν_{res} is plotted as a function of the electric field E_3 in the substrate and film thickness t_f. Such maps are developed with the account of the equilibrium magnetization orientation, which is calculated by numerical minimization of the energy density $\Delta F(\theta, \varphi)$ and determined as a function of t_f and E_3. To comply with typical

FMR measurements, we assume that the film is subjected to a nonzero static magnetic field **H**.

When the substrate creates isotropic biaxial strain $u_1 = u_2$ in the film plane ($u_1^0 = u_2^0$, $d_{31} = d_{32}$, $\xi_1 = \xi_2$), the electric-field effect on the energy density $\Delta F(m_i)$ is governed by the term $\delta F_E = -B_1(1 + 2c_{12}/c_{11})\xi_1 d_{31} E_3 m_3^2$. Hence, the (t_f, E_3)–diagram of equilibrium magnetization orientations [34] and the FMR map can be constructed without specifying the substrate piezoelectric constants and strain-transfer parameters by using the normalized field intensity E_3/E_∞ with $E_\infty \sim 1/(\xi_1 d_{31})$. Such generalized orientational diagrams and FMR maps are calculated for Ni and Fe films coupled to piezoelectric substrates of the discussed type. To demonstrate the role of a size-induced polar SRT between the perpendicular-to-plane (PP) and in-plane (IP) magnetization directions, we employ the proximity parameter $(t_f - t_{001}^{**})/t_f$ instead of the absolute film thickness t_f. Here,

$$t_{001}^{**} = (K_s - K_{s\perp})\left[\frac{1}{2}\mu_0 M_s^2 (N_{11} + N_{12} - N_{33})\right.$$
$$\left. + B_1\left(1 + 2\frac{c_{12}}{c_{11}}\right)u_1^0 + K_{1\perp} + \frac{B_1^2}{6c_{11}}\right]^{-1} \quad (8)$$

is the critical film thickness at which the PP magnetization orientation becomes unstable with respect to rotations toward $\langle 110 \rangle$ directions in the absence of electric and magnetic fields [34]. Since the critical electric field E_{cr}^{**} inducing such instability at **H** = 0 is defined by the relation $E_{cr}^{**} = E_\infty (t_f - t_{001}^{**})/t_f$ with

$$E_\infty = -\frac{(1/2)\mu_0 M_s^2 (N_{11} + N_{12} - N_{33}) + B_1(1 + 2c_{12}/c_{11})u_1^0 + K_{1\perp} + B_1^2/(6c_{11})}{B_1(1 + 2c_{12}/c_{11})\xi_1 d_{31}}, \quad (9)$$

the characteristic field E_∞ governing the normalized field intensity E_3/E_∞ is set equal to the quantity given by Eq. (9). In the numerical calculations, we disregard the

anticipated thickness dependence of the magnetoelastic coefficient $B_1 = B_1^b + B_1^s/t_f$ [36], because, in the considered case of thickness-independent strains $u_1 = u_2$, the

introduction of the term B_1^s/t_f just modifies the meaning of the surface/interface anisotropy constant K_s involved in Eq. (1).

We considered Ni films epitaxially grown on a thick (001)-oriented Cu buffer layer ($u_1^0 = u_2^0 \cong 2.58\%$) because the magnetic anisotropy constants of Ni(001)/Cu(001) heterostructures were measured experimentally [33,40]. The full set of material parameters [33,40–42], which is employed for Ni films in the numerical calculations, is given in Table I. Figure 2(a) shows the (t_f, E_3)–diagram of equilibrium magnetization orientations in strained Ni films subjected to the static magnetic field $H_1 = 100$ Oe. This diagram differs from the previously reported one [34] because we introduce a nonzero magnetic field and disregard the metastable states. The magnetic field applied along the [100] crystallographic direction enlarges the stability range of the [100] magnetization orientation and induces deviations from the [110] and [001] directions stable at $\mathbf{H} = 0$ (see Appendix for the critical thicknesses of FM films subjected to external magnetic fields). As a result, four different orientational states appear in the orientational diagram, which are denoted by the letters a (direction cosines $m_1 = 1$ and $m_2 = m_3 = 0$), ab ($m_1 \neq m_2 \neq 0$, $m_3 = 0$), ac ($m_1 \neq 0$, $m_2 = 0$, $m_3 \neq 0$), and abc ($m_1 \neq 0$, $m_2 \neq 0$, $m_3 \neq 0$) for brevity. The stability ranges of these states are separated by lines of continuous (second-order) or abrupt (first-order) SRTs. As seen from Fig. 2(a), both IP and polar SRTs appear upon changing the film thickness, whereas the electric field can induce only polar SRTs in the considered case of a piezoelectric substrate creating isotropic biaxial strain $u_1 = u_2$ in the film.

The generalized FMR map of ultrathin Ni films calculated with the account of their orientational diagram is shown in Fig. 2(b). Remarkably, the FMR map clearly demonstrates the presence of SRTs, which manifest themselves in dark streaks indicating drastically reduced resonance frequency. On the other hand, FMR frequency ν_{res} strongly increases at negative electric fields E_3 and thicknesses $t_f > t_{001}^{**}$, exceeding 7 GHz under certain conditions. To evaluate the efficiency of electric-field control of ν_{res}, we calculate the tunability $\partial\nu_{res}/\partial E_3$ of the resonance frequency. Figure 3 shows the tunability map of Ni films together with representative dependences of the normalized tunability $\partial\nu_{res}/\partial(E_3/E_\infty)$ on the proximity parameter $(t_f - t_{001}^{**})/t_f$ and the normalized field E_3/E_∞. As can be seen from Fig. 3(a), absolute values of tunability increase drastically near the lines of polar SRTs, which border the stability range of the abc magnetic state. At the first-order $ab\leftrightarrow abc$ transition, the normalized tunability increases up to about 1000 GHz/E_∞, whereas at the second-order $abc\leftrightarrow ac$ transition, it diverges in our approximation while the FMR frequency goes to zero [see panels (b) and (c) in Fig. 3].

The actual tunabilities $\partial\nu_{res}/\partial E_3$ of the FMR frequency in Ni films coupled to various piezoelectric and
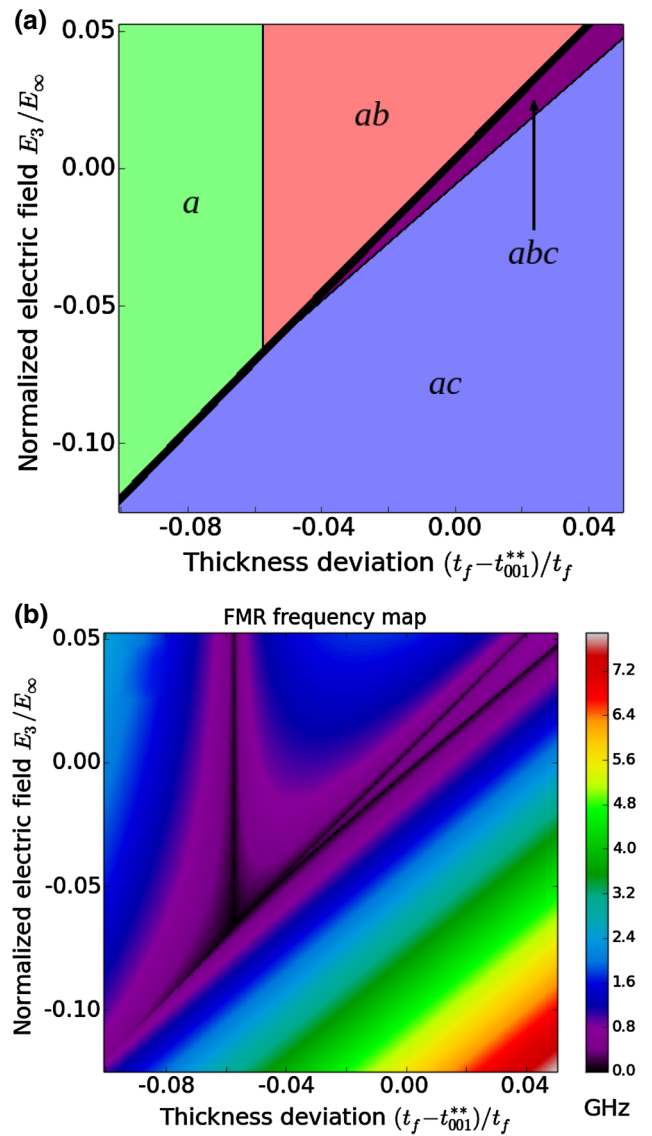

FIG. 2. Diagram of equilibrium magnetization orientations (a) and FMR frequency map (b) calculated for ultrathin Ni films coupled to piezoelectrically active substrates creating isotropic biaxial strain $u_1 = u_2$ in the film plane. The application of a static magnetic field $H_1 = 100$ Oe along the [100] crystallographic direction is assumed in the calculations. The electric field intensity E_3 is normalized by the quantity E_∞ given by Eq. (9), and the film thickness t_f is counted from the critical value t_{001}^{**} defined by Eq. (8). The demagnetizing factors and initial lattice strains are assumed to be $N_{11} = N_{22} = N_{12} = 0$, $N_{33} = 1$, and $u_1^0 = u_2^0 = 0.0258$. Continuous (second-order) and abrupt (first-order) SRTs are denoted by thin and thick lines, respectively.

ferroelectric substrates can be evaluated using the values of the characteristic field E_∞ given in Table II, which are calculated from Eq. (9) at $N_{11} = N_{12} = 0$, $N_{33} = 1$, $u_1^0 = 2.58\%$, and $\xi_1 = 1$. In these calculations, we employ the measured piezoelectric constants $d_{31} = d_{32}$ of representative piezoelectric crystals AlN
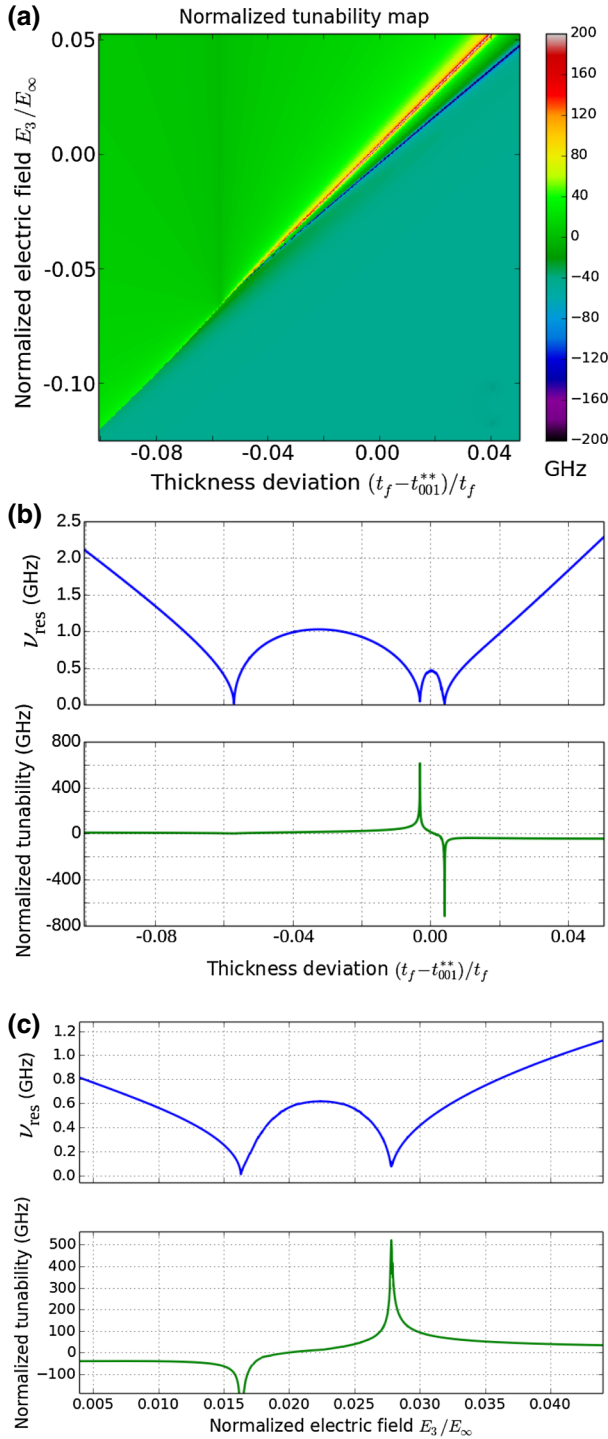
FIG. 3. Electrical tunability of FMR frequency calculated for ultrathin Ni films coupled to piezoelectric substrates creating isotropic biaxial strain in the film plane. Panel (a) demonstrates the map of normalized tunability $\partial \nu_{\rm res}/\partial(E_3/E_\infty)$, which corresponds to the FMR map presented in Fig. 2(b). Panel (b) shows the dependences of FMR frequency $\nu_{\rm res}$ and normalized tunability on the film thickness at zero electric field, while panel (c) presents variations of $\nu_{\rm res}$ and $\partial \nu_{\rm res}/\partial(E_3/E_\infty)$ with the intensity E_3 at the proximity parameter $(t_f - t_{001}^{**})/t_f = 0.02$. The electric field E_3 is normalized by the intensity E_∞ given by Eq. (9).

and ZnO [43,44], classical ferroelectrics PbTiO$_3$ and BaTiO$_3$ [45], lead zirconate titanate (PZT) solid solution [46], and relaxor-based ferroelectric single crystals Pb(Mg$_{1/3}$Nb$_{2/3}$)O$_3$–30%PbTiO$_3$ (PMN-30%PT) and Pb(Zn$_{1/3}$Nb$_{2/3}$)O$_3$–8%PbTiO$_3$ (PZN-8%PT) [47]. Since the actual tunability is given by the normalized tunability $\partial \nu_{\rm res}/\partial(E_3/E_\infty)$ divided by E_∞, the data presented in Table II demonstrate that $\partial \nu_{\rm res}/\partial E_3$ is maximal for Ni films integrated onto relaxor ferroelectrics and minimal for those coupled to conventional piezoelectrics AlN and ZnO. At the $ab \leftrightarrow abc$ transition line, for instance, the tunability of Ni films grown on the Cu-buffered PMN-30%PT or PZN-8%PT crystals reaches values above 8 GHz/(kV/cm), which greatly exceeds the maximal tunability $|\partial \nu_{\rm res}/\partial E_3| \approx 0.23$ GHz/(kV/cm) predicted for thick Ni films [21].

For the PP magnetization orientations ($\theta = \theta_H = 0$), an analytic expression for the tunability can be derived via the differentiation of Eq. (4). The calculation shows that such an expression is generally very cumbersome, but in the particular case of $N_{11}^* = N_{22}^*$ and $N_{12}^* = 0$ it reduces to a simple formula

$$\frac{\partial \nu_{\rm res}}{\partial E_3} = \frac{\gamma}{\pi M_s}\left(1 + \frac{2c_{12}}{c_{11}}\right)\xi_1 B_1 d_{31}, \qquad (10)$$

which, at $\xi_1 = 1$, coincides with the relation obtained earlier [21]. The tunabilities calculated from Eq. (10) for perpendicularly magnetized Ni films coupled to various piezoelectric substrates are given in Table II. It can be seen that $|\partial \nu_{\rm res}/\partial E_3|$ remains below 0.4 GHz/(kV/cm) even for Ni films integrated onto relaxor ferroelectrics PMN-30%PT and PZN-8%PT.

The generalized orientational diagram and FMR map are also computed for ultrathin Fe films epitaxially grown on a thick, fully relaxed MgO buffer layer ($u_1^0 = u_2^0 \cong 3.9\%$). Here, we use the material parameters of Fe films [41,42,48] listed in Table I, some of which are extracted from the experimental data available for MgO/Fe/MgO heterostructures [48]. Figure 4(a) demonstrates the (t_f, E_3)–diagram of equilibrium magnetization orientations in strained Fe films subjected to the static magnetic field of 100 Oe applied along the [110] crystallographic direction. The diagram comprises stability ranges of the aa ($m_1 = m_2 \neq 0$, $m_3 = 0$), ab ($m_1 \neq m_2 \neq 0$, $m_3 = 0$), and aac ($m_1 = m_2 \neq 0$, $m_3 \neq 0$) orientational states only, because the c state ($m_1 = m_2 = 0$, $m_3 = 1$) existing at **H** = 0 [34] transforms into the aac one in the presence of a magnetic field with $H_1 = H_2 \neq 0$. As in the case of Ni films, the isotropic biaxial strain $\delta u_1(E_3) = \delta u_2(E_3)$ created by a piezoelectric substrate can induce only a polar SRT. However, this SRT is always of the first order in Fe films, as demonstrated by Fig. 4(a). The corresponding FMR map shown in Fig. 4(b) displays regions of strongly reduced resonance frequency, which are located at the SRT lines.

TABLE II.   Characteristic electric fields of Ni/Cu and Fe/MgO heterostructures coupled to piezoelectric and ferroelectric substrates creating biaxial isotropic strain in the overlayer and electrical tunabilities of FMR frequency calculated for perpendicularly magnetized (pm) Ni and Fe films.

Substrate	$d_{31} = d_{32}$ (pm/V)	E_∞ of Ni/Cu (MV/cm)	E_∞ of Fe/MgO (MV/cm)	$\partial\nu_{res}/\partial E_3$ of pm-Ni (GHz/kV/cm)	$\partial\nu_{res}/\partial E_3$ of pm-Fe (GHz/kV/cm)
AlN	−2 [43]	84	1370	-5×10^{-4}	5×10^{-5}
ZnO	−5 [44]	33	550	-1.3×10^{-3}	1.2×10^{-4}
PbTiO₃	−28 [45]	6	98	-7.5×10^{-3}	6.7×10^{-4}
BaTiO₃	−36 [45]	4.6	76	-9.7×10^{-3}	8.7×10^{-4}
PZT-5H	−274 [46]	0.6	10	-7.4×10^{-2}	6.6×10^{-3}
PMN-30%PT	−1395 [47]	0.12	2	−0.38	3.4×10^{-2}
PZN-8%PT	−1455 [47]	0.115	1.9	−0.39	3.5×10^{-2}

Far from these lines, the FMR frequency varies in the GHz range, increasing up to 20 GHz at thicknesses $t_f < 0.95 t_{001}^{**}$ and strong positive electric fields $E_3 > 0.2 E_\infty$.

The tunability map of ultrathin Fe films is shown in Fig. 5 together with representative dependences of the normalized tunability $\partial\nu_{res}/\partial(E_3/E_\infty)$ on the proximity parameter $(t_f - t_{001}^{**})/t_f$ and the normalized electric field E_3/E_∞. As can be seen from Fig. 5(a), the tunability $\partial\nu_{res}/\partial E_3$ is comparatively high and practically constant inside the stability range of the *aac* orientational state, exceeding 60 GHz/E_∞ far from the *aac*→*aa* transition line. In contrast, absolute values of the tunability are rather small within the stability ranges of the *aa* and *ab* states, except for the region near the *aa*→*aac* transition line, where $\partial\nu_{res}/\partial E_3$ reaches −70 GHz/E_∞ [see Figs. 5(b) and 5(c)]. It should be noted that the *aa* state is distinguished by a nonmonotonic variation of the FMR frequency with the film thickness, which is illustrated in Fig. 5(b). Furthermore, no significant enhancement of the tunability magnitude $|\partial\nu_{res}/\partial E_3|$ takes place at the *aa*↔*ab* transition line, because this SRT occurs at a critical thickness independent of the electric field E_3 [see Fig. 4(a)].

The actual tunabilities $\partial\nu_{res}/\partial E_3$ of the FMR frequency in Fe films coupled to different piezoelectrically active substrates can be evaluated using the values of the electric field E_∞ listed in Table II, which are calculated from Eq. (9) at $N_{11} = N_{12} = 0$, $N_{33} = 1$, $u_1^0 = 3.9\%$, and $\xi_1 = 1$. The inspection of Table II demonstrates that the characteristic fields E_∞ of Fe films are much higher than those of Ni films coupled to the same substrate. This feature is due to the four times larger magnetization M_s of iron and the smaller absolute value of its magnetoelastic constant B_1 (see Table I). Owing to higher characteristic fields E_∞, tunabilities of Fe films appear to be rather low in comparison with those of Ni films. For instance, the normalized tunability of −70 GHz/E_∞ predicted above for the region near the *aa*→*aac* transition line yields only $\partial\nu_{res}/\partial E_3 \approx -3.5 \times 10^{-2}$ GHz/(kV/cm) for Fe films coupled to PMN-30%PT or PZN-8%PT. Similarly, the

tunabilities of perpendicularly magnetized Fe films calculated from Eq. (10) are about 10 times smaller than $|\partial\nu_{res}/\partial E_3|$ of Ni films on the same substrate (see Table II).

To exemplify the case of piezoelectric substrates creating anisotropic strains $\delta u_1(E_3) \neq \delta u_2(E_3)$ in the FM overlayer, we calculate the orientational diagram and the FMR map for ultrathin Fe₆₀Co₄₀ layers coupled to the (011)-cut PZN-6%PT single crystal poled along the [011] pseudocubic direction. At this orientation, the PZN-6%PT substrate has very different piezoelectric coefficients $d_{31} = -3000$ pm/V and $d_{32} = 1100$ pm/V [23], which render it possible to generate anisotropic IP strains even by an electric field orthogonal to the substrate surface (Fig. 1). In the numerical calculations, we use the set of material parameters given in Table I, which characterizes the properties of Fe₆₀Co₄₀ films at room temperature [42,49–52]. Figure 6(a) presents the (t_f, E_3)–diagram of equilibrium magnetization orientations in initially unstrained ($u_1^0 = u_2^0 = 0$) Fe₆₀Co₄₀ layers subjected to a static magnetic field $H_1 = 100$ Oe parallel to the [100] crystallographic axis. The diagram involves stability ranges of the *a*, *ab*, and *ac* orientational states, which are separated by the lines of first-order SRTs. Since an electrically biased PZN-6%PT substrate generates unequal strains $\delta u_1(E_3) \neq \delta u_2(E_3)$ in the Fe₆₀Co₄₀ overlayer, even magnetization reorientations in the layer plane could be induced by the applied voltage. Importantly, at Fe₆₀Co₄₀ thicknesses close to the critical thickness t_{001}^{**}, both IP and polar SRTs arise at weak electric fields of a few kV/cm, which do not lead to the polarization reversal and phase transitions in the relaxor ferroelectric PZN-6%PT [23].

The FMR map of Fe₆₀Co₄₀ layers demonstrates strong variations of the resonance frequency within the considered region of the (t_f, E_3)–plane [see Fig. 6(b)]. The FMR frequency reduces down to 0.16 GHz at the triple point in the orientational diagram shown in Fig. 6(a) and increases up to 2–3 GHz far from the SRT lines. The corresponding tunability map and representative dependences of $\partial\nu_{res}/\partial E_3$ on the proximity parameter $(t_f - t_{001}^{**})/t_f$
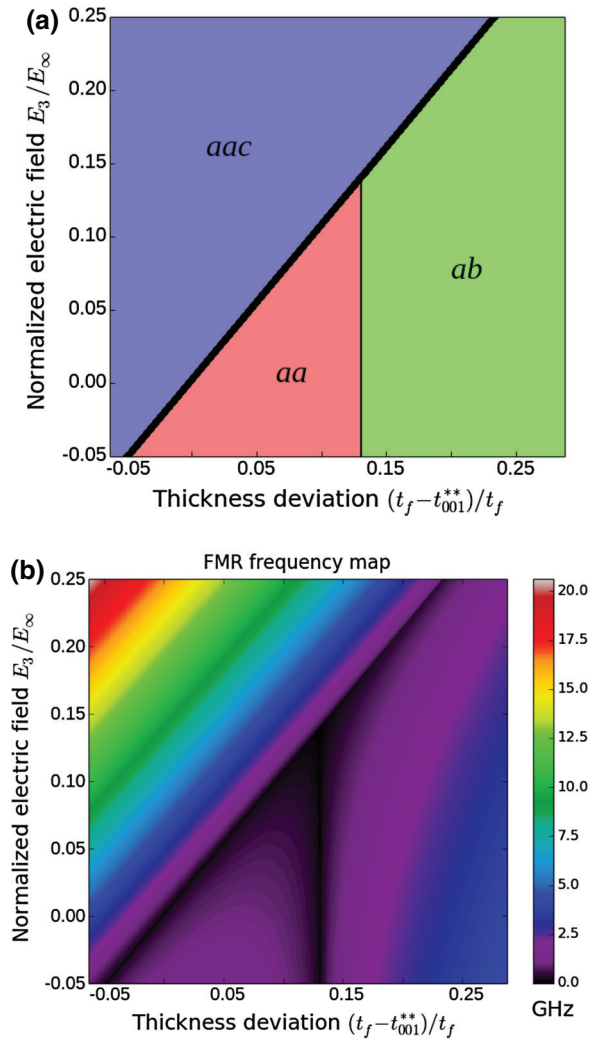
(a)

(b) FMR frequency map

FIG. 4.   Diagram of equilibrium magnetization orientations (a) and FMR frequency map (b) of ultrathin Fe films coupled to piezoelectrically active substrates creating isotropic biaxial strain $u_1 = u_2$ in the film plane. Films are subjected to a static magnetic field of 100 Oe applied along the [110] crystallographic direction. The electric field intensity E_3 is normalized by the quantity E_∞ given by Eq. (9), and the film thickness t_f is counted from the critical value t_{001}^{**} defined by Eq. (8). The demagnetizing factors and initial lattice strains are assumed to be $N_{11} = N_{22} = N_{12} = 0$, $N_{33} = 1$, and $u_1^0 = u_2^0 = 0.039$.

and electric field intensity E_3 are presented in Fig. 7. It is seen that the tunability is positive within the stability ranges of the *ab* and *ac* states and negative for the *a* state [Fig. 7(a)]. On crossing the *a↔ac* and *a↔ab* transition lines, $\partial\nu_{\mathrm{res}}/\partial E_3$ experiences steplike changes and may significantly increase in magnitude in the vicinity of these lines [see Figs. 7(b) and 7(c)]. Remarkably, the tunability magnitude $|\partial\nu_{\mathrm{res}}/\partial E_3|$ exceeds 1 GHz/(kV/cm) near the *a↔ab* transition line at the [100] magnetization orientation, which is five times larger than the value of 0.18 GHz/(kV/cm) predicted for thick $Fe_{60}Co_{40}$ films [21].

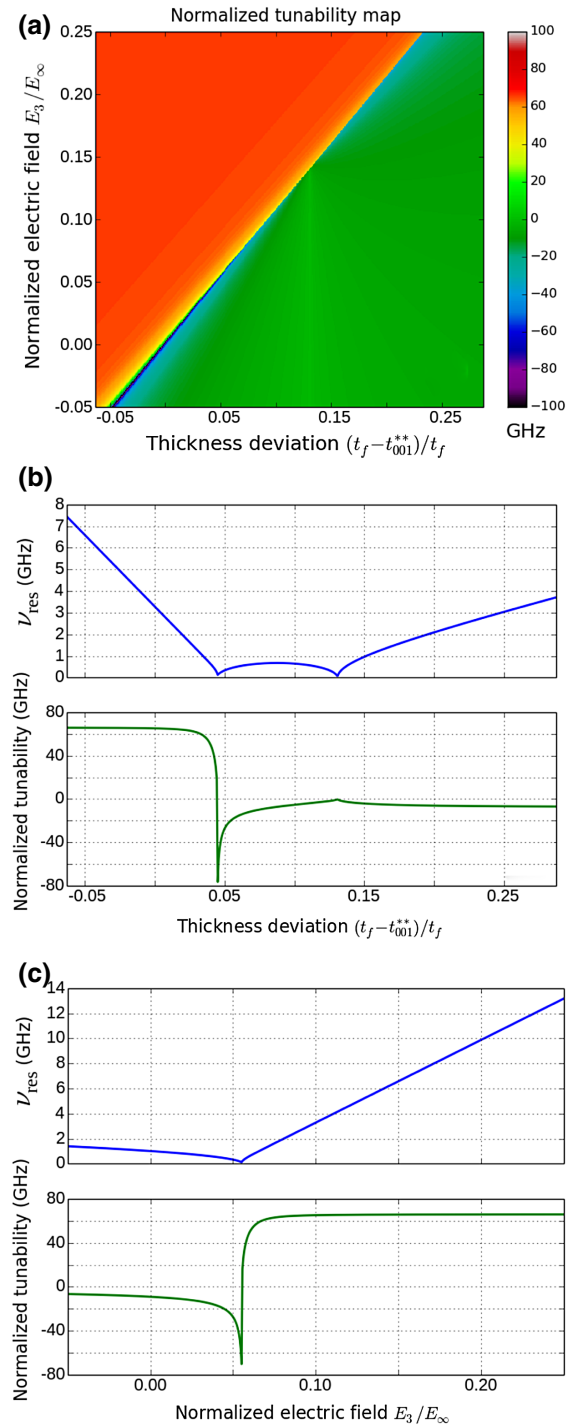**(a)** Normalized tunability map

(b)

(c)

FIG. 5.   Electrical tunability of FMR frequency calculated for ultrathin Fe films coupled to piezoelectric substrates creating isotropic biaxial strain in the film plane. Panel (a) demonstrates the map of normalized tunability $\partial\nu_{\mathrm{res}}/\partial(E_3/E_\infty)$, which corresponds to the FMR map presented in Fig. 4(b). Panel (b) shows the dependences of FMR frequency ν_{res} and normalized tunability on the film thickness at the electric field $E_3 = 0.05 E_\infty$, while panel (c) presents variations of ν_{res} and $\partial\nu_{\mathrm{res}}/\partial(E_3/E_\infty)$ with the field intensity E_3 at the proximity parameter $(t_f - t_{001}^{**})/t_f = 0.05$. The electric field E_3 is normalized by the intensity E_∞ given by Eq. (9).
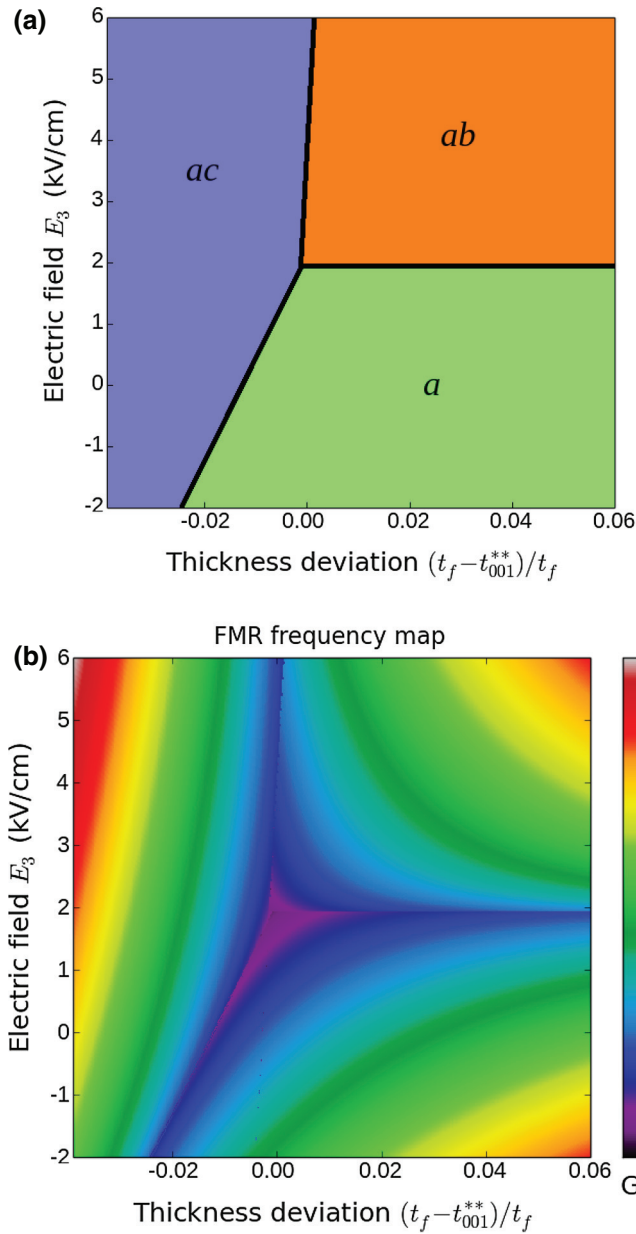
FIG. 6. Diagram of equilibrium magnetization orientations (a) and FMR frequency map (b) calculated for ultrathin $Fe_{60}Co_{40}$ layers coupled to the (011)-cut PZN-6%PT single crystal poled along the [011] pseudocubic direction. The static magnetic field $H_1 = 100$ Oe is parallel to the [100] crystallographic axis. The film thickness t_f is counted from the critical value t_{001}^* defined by Eq. (8). The demagnetizing factors and initial lattice strains are assumed to be $N_{11} = 0.005$, $N_{22} = 0.01$, $N_{12} = 0$, $N_{33} = 0.985$, and $u_1^0 = u_2^0 = 0$, while the strain transfer parameters ξ_1 and ξ_2 are set to unity.

In contrast, the tunability remains below 0.1 GHz/(kV/cm) near the $ab \leftrightarrow ac$ transition line, along which the critical thickness rather weakly varies with the electric field [Fig. 7(a)].
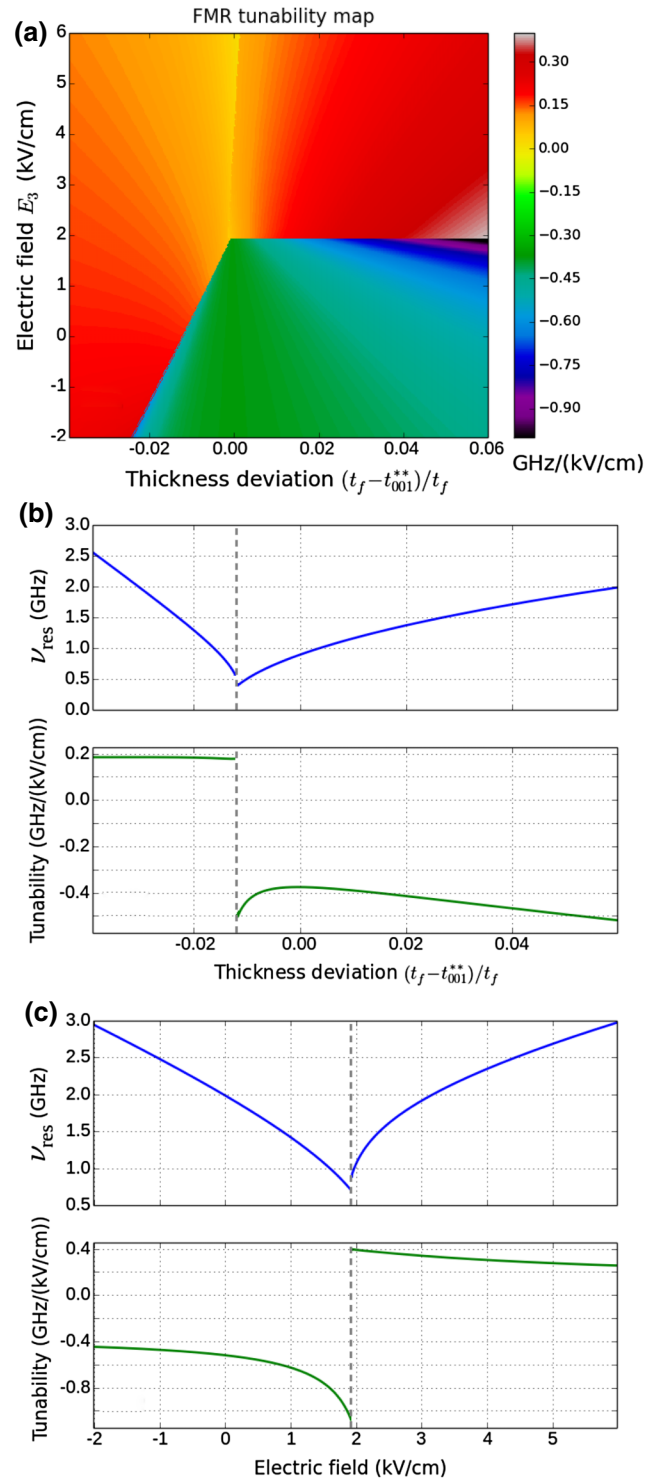

FIG. 7. Electrical tunability of FMR frequency calculated for ultrathin $Fe_{60}Co_{40}$ films coupled to the (011)-cut PZN-6%PT single crystal poled along the [011] pseudocubic direction. Panel (a) shows the map of tunability $\partial \nu_{res}/\partial E_3$, which corresponds to the FMR map presented in Fig. 6(b). Panel (b) demonstrates the dependences of FMR frequency ν_{res} and tunability on the film thickness at zero electric field, while panel (c) presents variations of ν_{res} and $\partial \nu_{res}/\partial E_3$ with the field intensity E_3 at the proximity parameter $(t_f - t_{001}^{**})/t_f = 0.06$.

IV. CONCLUSIONS

In this paper, we theoretically describe the strain effects on the FMR of thin-film nanomagnets, which result from the magnetoelastic coupling between spins and lattice deformations. The FMR frequency of a strained nanomagnet is calculated analytically with the account of second-order and fourth-order terms in the series expansion of the surface/interface magnetic anisotropy. The derived general relation is valid for ultrathin FM films and islands homogeneously magnetized in an arbitrary direction, as confirmed by numerical simulations performed in macrospin approximation. Importantly, this analytical relation, which allows for both the size and strain effects on the resonance frequency and field, facilitates analysis of FMR data measured for thin-film nanomagnets coupled to substrates of any type (passive or active). The theoretical results obtained for the strain and size effects on the FMR frequency are used to quantify the strain-mediated electric-field control of FMR in thin-film nanomagnets mechanically coupled to piezoelectrically active substrates. This converse magnetoelectric effect is described by calculating the FMR frequency ν_{res} and its electrical tunability $\partial \nu_{res}/\partial E_3$ as a function of the nanomagnet thickness t_f and the electric field E_3 created in the substrate by a voltage source.

The numerical calculations are performed for ultrathin Ni, Fe, and $Fe_{60}Co_{40}$ layers integrated onto AlN and ZnO wurtzite crystals, classical ferroelectrics $PbTiO_3$ and $BaTiO_3$, ferroelectric solid solution PZT, and relaxor ferroelectrics PMN-PT and PZN-PT. In these calculations, the substrate-induced strains in the FM overlayer are assumed to vary linearly with the field intensity E_3 in accordance with the substrate piezoelectric coefficients d_{31} and d_{32}. The results are presented in the form of two-dimensional maps showing variations of the energetically most favorable magnetization orientation, resonance frequency, and its electrical tunability in the (t_f, E_3)–plane (Figs. 2–7). Such maps can be constructed for thin-film nanomagnets coupled to ferroelectric substrates experiencing nonlinear and hysteretic piezoelectric deformations as well. This can be achieved by using electric-field dependences of the IP film strains corresponding to experimentally measured variations of substrate deformations [23,28,38,53]. It should be emphasized that, using the data given in Table II and the generalized orientational diagrams, which were constructed for magnetically biased Ni and Fe films coupled to piezoelectrically active substrates creating isotropic biaxial strain in the film plane [Figs. 2(a) and 4(a)], it is possible to compare the efficiency of different substrates for the strain-mediated electrical control of magnetic states.

The developed (t_f, E_3)–maps demonstrate that the FMR frequency and its electrical tunability are highly sensitive to both nanomagnet thickness and substrate-induced lattice strains. This feature is due to the presence of size-induced and strain-driven SRTs in ultrathin FM layers. Indeed, the FMR frequency diminishes in the vicinity of SRT lines on the (t_f, E_3)–plane, which is accompanied by the drastic increase in the tunability at most SRTs driven or shifted by lattice strains. The numerical estimates further show that multiferroic heterostructures involving relaxor ferroelectrics with ultrahigh piezoelectric coefficients are most efficient for the strain-mediated electrical tuning of FMR. For instance, $Fe_{60}Co_{40}$ layers coupled to the (011)-cut and [011]-poled PZN-6%PT single crystal have $|\partial \nu_{res}/\partial E_3| > 1$ GHz/(kV/cm) at the IP SRT induced by anisotropic strains $u_1 \neq u_2$. Moreover, the tunability of FMR frequency in Ni films grown on the Cu-buffered PMN-30%PT or PZN-8%PT crystals exceeds 8 GHz/(kV/cm) at the polar first-order SRT. These theoretically predicted tunabilities are comparable with the experimental values obtained for the $(Fe_{100-y}Ga_y)_{1-x}B_x$/PZN-6%PT hybrid, which exhibits a mean tunability of about 1 GHz/(kV/cm) and a rise of $\partial \nu_{res}/\partial E_3$ up to 15 GHz/(kV/cm) at the electric-field-induced phase transition occurring in the PZN-6%PT single crystal at $E_3 \approx 6$ kV/cm [23].

Regarding the strain-mediated electrical tuning of FMR, it should be also noted that the field-induced substrate deformations are limited by two factors. First, the electric field in any substrate cannot exceed the dielectric breakdown field E_b. Second, if the electric field in ferroelectric material is directed against the spontaneous polarization, the substrate deformations stop to develop monotonically when the field intensity reaches the coercive field E_c, at which the polarization reversal takes place. In the case of PMN-PT and PZN-PT crystals, the breakdown field is rather high ($E_b > 100$ kV/cm), but the coercive field is only approximately 2 kV/cm [54]. These limits are satisfied in the (t_f, E_3)–maps shown in Figs. 6 and 7, and similar restrictions should be taken into account when applying the generalized maps presented in Figs. 2–5 to Ni and Fe films coupled to particular ferroelectric substrates.

In general, the FMR frequency of a thin-film nanomagnet integrated onto a biased ferroelectric substrate should be additionally affected by electric-field-induced variations in the interfacial magnetic anisotropy of the FM overlayer. Such interfacial contribution to the electrical tuning of FMR has been demonstrated experimentally by comparing the FMR data obtained for NiFe/PMN-PT and NiFe/Cu/PMN-PT multiferroic heterostructures [55]. It appears in the case of direct contact between FM layer and a ferroelectric or dielectric material having voltage-dependent polarization along the normal to the interface, being due to the polarization-dependent interfacial magnetic anisotropy [56]. Hence the FMR tuning of interfacial origin is absent for the Ni/Cu bilayers discussed in this paper, but it should be considered for

Fe/MgO and $Fe_{60}Co_{40}$ films if they are not separated from the substrate surface by a conductive nonmagnetic interlayer. The interfacial contribution to the electrical tuning of FMR can be incorporated into the present theory by introducing electric-field dependences of the coefficients K_s, $K_{s\parallel}$, and $K_{s\perp}$ involved in Eq. (1), which are controlled by the out-of-plane polarization $P_3(E_3)$ in the substrate.

Thus, our theoretical results demonstrate that multiferroic heterostructures in the form of thin-film nanomagnets with strong magnetoelastic coupling integrated onto ferroelectric substrates are promising for the development of electrically tunable linear and nonlinear rf/microwave devices with high tuning speed and low energy consumption. Possible device applications of such hybrids include magnetoelectric bandpass filters, phase shifters, resonators, delay lines [57–60], frequency-tunable resonant antennas, parametric circuits, mixers, and frequency multipliers [21].

APPENDIX

Energetically most favorable magnetization orientations in strained ultrathin layers of cubic ferromagnets can be found via the minimization of the effective volumetric energy density ΔF given by Eq. (1). When such orientation is parallel to one of the edges of the unit cell or to its IP face diagonal, it is possible to derive analytical relations for the critical layer thicknesses, at which the magnetization vector loses stability against rotation toward another spatial direction. The derivation involves the analysis of the Hessian matrix of the function $\Delta F(\theta, \varphi)$ written in terms of polar angle θ and azimuth angle φ defining the magnetization direction in the spherical coordinate system. Analytical results obtained for the critical thicknesses of ultrathin FM layers subjected to an external magnetic field **H** and thickness-independent IP strains **u** are given below.

(i) If the total magnetic anisotropy of the FM layer favors IP magnetization orientation along the [100] crystallographic axis, the magnetization retains such orientation in the presence of a magnetic field provided that the vector **H** is orthogonal to the (100) plane ($H_1 \neq 0$, $H_2 = H_3 = 0$). For critical thicknesses at which the [100] magnetization orientation loses stability against IP and out-of-plane rotations, the calculations yield the relations

$$t_{100}^* = -\frac{K_{s\parallel}}{(1/2)\mu_0 M_s^2(N_{22} - N_{11}) + B_1(u_2 - u_1) + K_{1\parallel} + (1/2)\mu_0 M_s H_1}, \tag{A1}$$

$$t_{100}^{**} = \frac{K_s + K_{s\perp}}{(1/2)\mu_0 M_s^2(N_{11} - N_{33}) + B_1[u_1 + (c_{12}/c_{11})(u_1 + u_2)] - K_{1\perp} + (B_1^2/6c_{11}) - (1/2)\mu_0 M_s H_1}, \tag{A2}$$

which are valid at $\mu_0 M_s^2 N_{11} + 2B_1 u_1 \leq \mu_0 M_s^2 N_{22} + 2B_1 u_2$ and $\mu_0 M_s^2 N_{12} + B_2 u_6 = 0$ only.

(ii) When the total magnetic anisotropy of the FM layer favors IP magnetization orientation along the [110] direction, the magnetization has such orientation only if the magnetic field **H** is also parallel to this direction

($H_1 = H_2 = H$, $H_3 = 0$). The critical thicknesses at which the [110] magnetization orientation loses stability against IP and out-of-plane rotations are given by the formulas

$$t_{110}^* = -\frac{K_{s\parallel}}{\mu_0 M_s^2 N_{12} + B_2 u_6 + K_{1\parallel} - (1/\sqrt{2})\mu_0 M_s H}, \tag{A3}$$

$$t_{110}^{**} = \frac{K_s + K_{s\perp} - (K_{s\parallel}/2)}{(1/2)\mu_0 M_s^2(N_{11} + N_{12} - N_{33}) + B_1[u_1 + (c_{12}/c_{11})(u_1 + u_2)] + (B_2/2)u_6 + (K_{1\parallel}/2) - K_{1\perp} - (K_2/4) + (B_1^2/6c_{11}) - (1/\sqrt{2})\mu_0 M_s H}, \tag{A4}$$

which imply that the conditions $\mu_0 M_s^2(N_{11} - N_{22}) = 2B_1(u_2 - u_1)$ and $\mu_0 M_s^2 N_{12} + B_2 u_6 \leq 0$ are satisfied.

(iii) In the presence of magnetic field **H** parallel or antiparallel to the [001] crystallographic direction ($H_1 = H_2 = 0$, $H_3 \neq 0$), the magnetization will be oriented exactly along **H** if the total magnetic anisotropy of the

FM layer favors the PP magnetization orientation. The critical thickness at which the PP orientation should lose its stability against reorientation toward the energetically most favorable IP direction depends on the IP magnetic anisotropy. If such a direction is parallel to the [100] axis, which may happen only at $\mu_0 M_s^2 N_{11} + 2B_1 u_1 \leq \mu_0 M_s^2 N_{22} + 2B_1 u_2$ and $\mu_0 M_s^2 N_{12} + B_2 u_6 = 0$, the critical thickness equals

$$t^*_{001} = \frac{K_s - K_{s\perp}}{(1/2)\mu_0 M_s^2(N_{11} - N_{33}) + B_1[u_1 + (c_{12}/c_{11})(u_1 + u_2)] + K_{1\perp} + (B_1^2/6c_{11}) + (1/2)M_s H_3}. \tag{A5}$$

When the magnetization reorientation occurs toward the [110] crystallographic direction, the critical thickness is given by the formula

$$t^{**}_{001} = \frac{K_s - K_{s\perp}}{(1/2)\mu_0 M_s^2(N_{11} + N_{12} - N_{33}) + B_1[u_1 + (c_{12}/c_{11})(u_1 + u_2)] + (1/2)B_2 u_6 + K_{1\perp} + (B_1^2/6c_{11}) + (1/2)\mu_0 M_s H_3}, \tag{A6}$$

which is valid at $\mu_0 M_s^2(N_{11} - N_{22}) = 2B_1(u_2 - u_1)$ and $\mu_0 M_s^2 N_{12} + B_2 u_6 \leq 0$ only.

In the case of FM layers not subjected to a magnetic field ($H_1 = H_2 = H_3 = 0$), the whole set of Eqs. (A1)–(A6) can be used to predict the existence of SRTs and to determine their order as described in Ref. [34]. If the magnetic field is significant, only two of these equations remain valid at best [e.g., Eqs. (A5) and (A6) at $H_1 = H_2 = 0$, $H_3 \neq 0$] so that SRTs cannot be located and characterized without the numerical minimization of the free energy density $\Delta F(\theta, \varphi)$.

[1] T. G. Philipps and H. M. Rosenberg, Spin waves in ferromagnets, Rep. Prog. Phys. **29**, 285 (1966).

[2] B. Heinrich and J. F. Cochran, Ultrathin metallic magnetic films: magnetic anisotropies and exchange interactions, Adv. Phys. **42**, 523 (1993).

[3] M. Farle, Ferromagnetic resonance of ultrathin metallic layers, Rep. Prog. Phys. **61**, 755 (1998).

[4] H. How, W. Hu, C. Vittoria, L. C. Kempel, and K. D. Trott, Single-crystal yttrium iron garnet phase shifter at X band, J. Appl. Phys. **85**, 4853 (1999).

[5] N. Cramer, D. Lucic, R. E. Camley, and Z. Celinski, High attenuation tunable microwave notch filters utilizing ferromagnetic resonance, J. Appl. Phys. **87**, 6911 (2000).

[6] J. D. Adam and S. N. Stitzer, A magnetostatic wave signal-to-noise enhancer, Appl. Phys. Lett. **36**, 485 (1980).

[7] Y. V. Khivintsev, V. V. Zagorodnii, A. J. Hutchison, R. E. Camley, and Z. J. Celinski, On-wafer microwave signal-to-noise enhancer using NiFe films, Appl. Phys. Lett. **92**, 022512 (2008).

[8] M. Weiler, L. Dreher, C. Heeg, H. Huebl, R. Gross, M. S. Brandt, and S. T. B. Goennenwein, Elastically Driven Ferromagnetic Resonance in Nickel Thin Films, Phys. Rev. Lett. **106**, 117601 (2011).

[9] L. Dreher, M. Weiler, M. Pernpeintner, H. Huebl, R. Gross, M. S. Brandt, and S. T. B. Goennenwein, Surface acoustic wave driven ferromagnetic resonance in nickel thin films: Theory and experiment, Phys. Rev. B **86**, 134415 (2012).

[10] A. V. Azovtsev and N. A. Pertsev, Magnetization dynamics and spin pumping induced by standing elastic waves, Phys. Rev. B **94**, 184401 (2016).

[11] T. Nozaki, Y. Shiota, S. Miwa, S. Murakami, F. Bonell, S. Ishibashi, H. Kubota, K. Yakushiji, T. Saruya, A. Fukushima, S. Yuasa, T. Shinjo, and Y. Suzuki, Electric-field-induced ferromagnetic resonance excitation in an ultrathin ferromagnetic metal layer, Nat. Phys. **8**, 491 (2012).

[12] J. Zhu, J. A. Katine, G. E. Rowlands, Y.-J. Chen, Z. Duan, J. G. Alzate, P. Upadhyaya, J. Langer, P. K. Amiri, K. L. Wang, and I. N. Krivorotov, Voltage-Induced Ferromagnetic Resonance in Magnetic Tunnel Junctions, Phys. Rev. Lett. **108**, 197203 (2012).

[13] G. Viaud and N. A. Pertsev, Dynamic converse magnetoelectric effect in ferromagnetic nanostructures with electric-field-dependent interfacial anisotropy, Phys. Rev. B **90**, 064429 (2014).

[14] K. Miura, S. Yabuuchi, M. Yamada, M. Ichimura, B. Rana, S. Ogawa, H. Takahashi, Y. Fukuma, and Y. Otani, Voltage-induced magnetization dynamics in CoFeB/MgO/CoFeB magnetic tunnel junctions, Sci. Rep. **7**, 42511 (2017).

[15] S. I. Kiselev, J. C. Sankey, I. N. Krivorotov, N. C. Emley, R. J. Schoelkopf, R. A. Buhrman, and D. C. Ralph, Microwave oscillations of a nanomagnet driven by a spin-polarized current, Nature (London) **425**, 380 (2003).

[16] W. H. Rippard, M. R. Pufall, S. Kaka, S. E. Russek, and T. J. Silva, Direct-Current Induced Dynamics in Co$_{90}$Fe$_{10}$/Ni$_{80}$Fe$_{20}$ Point Contacts, Phys. Rev. Lett. **92**, 027201 (2004).

[17] M. Deac, A. Fukushima, H. Kubota, H. Maehara, Y. Suzuki, S. Yuasa, Y. Nagamine, K. Tsunekawa, D. D. Djayaprawira, and N. Watanabe, Bias-driven high-power microwave emission from MgO-based tunnel magnetoresistance devices, Nat. Phys. **4**, 803 (2008).

[18] G. Srinivasan, Magnetoelectric composites, Annu. Rev. Mater. Res. **40**, 153 (2010).

[19] M. I. Bichurin, I. A. Kornev, V. M. Petrov, A. S. Tatarenko, Yu. V. Kiliba, and G. Srinivasan, Theory of magnetoelectric effects at microwave frequencies in a piezoelectric/magnetostrictive multilayer composite, Phys. Rev. B **64**, 094409 (2001).

[20] Y. Chen, A. Yang, M. R. Paudel, S. Stadler, C. Vittoria, and V. G. Harris, Microwave magnetoelectric coupling and ferromagnetic resonance frequency tuning of a Co$_2$MnSb/GaAs/PZN-PT heterostructure, Phys. Rev. B **83**, 104406 (2011).

[21] N. A. Pertsev, H. Kohlstedt, and R. Knöchel, Ferromagnetic resonance in epitaxial films: Effects of lattice strains and voltage control via ferroelectric substrate, Phys. Rev. B **84**, 014423 (2011).

[22] Y. Chen, J. Wang, M. Liu, J. Lou, N. X. Sun, C. Vittoria, and V. G. Harris, Giant magnetoelectric coupling

and *E*-field tunability in a laminated Ni$_2$MnGa/lead-magnesium-niobate-lead titanate multiferroic heterostructure, Appl. Phys. Lett. **93**, 112502 (2008).

[23] J. Lou, M. Liu, D. Reed, Y. Ren, and N. X. Sun, Giant electric field tuning of magnetism in novel multiferroic FeGaB/lead zinc niobate–lead titanate (PZN-PT) heterostructures, Adv. Mater. **21**, 4711 (2009).

[24] M. Liu and N. X. Sun, Voltage control of magnetism in multiferroic heterostructures, Phil. Trans. R. Soc. A **372**, 20120439 (2014).

[25] Z. Hu, T. Nan, X. Wang, M. Staruch, Y. Gao, P. Finkel, and N. X. Sun, Voltage control of magnetism in FeGaB/PIN-PMN-PT multiferroic heterostructures for high-power and high-temperature applications, Appl. Phys. Lett. **106**, 022901 (2015).

[26] N. A. Pertsev, Giant magnetoelectric effect via strain-induced spin reorientation transitions in ferromagnetic films, Phys. Rev. B **78**, 212102 (2008).

[27] A. F. Andreev, Strictive superstructures in two-dimensional phase transitions, JETP Lett. **32**, 640 (1980).

[28] T. H. E. Lahtinen, K. J. A. Franke, and S. van Dijken, Electric-field control of magnetic domain wall motion and local magnetization reversal, Sci. Rep. **2**, 258 (2012).

[29] N. A. Pertsev, Strain-mediated electric-field control of multiferroic domain structures in ferromagnetic films, Appl. Phys. Lett. **102**, 112407 (2013).

[30] R. H. Wade, The determination of domain wall thickness in ferromagnetic films by electron microscopy, Proc. Phys. Soc. **79**, 1237 (1962).

[31] U. Gradmann, Magnetic surface anisotropies, J. Magn. Magn. Mater. **54–57**, 733 (1986).

[32] H. Fritzsche, J. Kohlhepp, H. J. Elmers, and U. Gradmann, Angular dependence of perpendicular magnetic surface anisotropy and the spin-reorientation transition, Phys. Rev. B **49**, 15665 (1994).

[33] M. Farle, B. Mirwald-Schulz, A. N. Anisimov, W. Platow, and K. Baberschke, Higher-order magnetic anisotropies and the nature of the spin-reorientation transition in face-centered-tetragonal Ni(001)/Cu(001), Phys. Rev. B **55**, 3708 (1997).

[34] N. A. Pertsev, Converse magnetoelectric effect via strain-driven magnetization reorientations in ultrathin ferromagnetic films on ferroelectric substrates, Phys. Rev. B **92**, 014416 (2015).

[35] C. Kittel, Physical theory of ferromagnetic domains, Rev. Mod. Phys. **21**, 541 (1949).

[36] G. Bochi, O. Song, and R. C. O' Handley, Surface magnetoelastic coupling coefficients of single-crystal fcc Co thin films, Phys. Rev. B **50**, 2043 (1994).

[37] N. A. Pertsev, Magnetic tunnel junction on a magnetostrictive substrate: An ultrasensitive magnetic-field sensor, Appl. Phys. Lett. **109**, 132406 (2016).

[38] T. Wu, A. Bur, W. Kin, Z. Ping, C. S. Lynch, P. K. Amiri, K. L. Wang, and G. P. Carman, Electrical control of reversible and permanent magnetization reorientation for magnetoelectric memory devices, Appl. Phys. Lett. **98**, 262504 (2011).

[39] Y. Shirahata, R. Shiina, D. L. González, K. J. A. Franke, E. Wada, M. Itoh, N. A. Pertsev, S. van Dijken, and T. Taniyama, Electric-field switching of perpendicularly magnetized multilayers, NPG Asia Mater. **7**, E198 (2015).

[40] R. Vollmer, Th. Gutjahr-Löser, J. Kirschner, S. van Dijken, and B. Poelsema, Spin-reorientation transition in Ni films on Cu(001): The influence of H$_2$ adsorption, Phys. Rev. B **60**, 6277 (1999).

[41] M. B. Stearns, in *Magnetic Properties of Metals· 3d, 4d, and 5d Elements, Alloys and Compounds*, Landolt-Börnstein, New Series, Group III, Vol. 19a (Springer-Verlag, Berlin, 1986). https://materials.springer.com/bp/docs/978-3-540-39667-3

[42] J. P. Hirth and J. Lothe, *Theory of Dislocations* (McGraw-Hill, New York, 1968).

[43] I. L. Guy, S. Muensit, and E. M. Goldys, Extensional piezoelectric coefficients of gallium nitride and aluminum nitride, Appl. Phys. Lett. **75**, 4133 (1999).

[44] D. F. Crisler, J. J. Cupal, and A. R. Moore, Dielectric, piezoelectric, and electromechanical coupling constants of zinc oxide crystals, Proc. IEEE **56**, 225 (1968).

[45] E. G. Fesenko, V. G. Gavrilyachenko, and A. F. Semenchev, *Domain Structure of Multiaxial Ferroelectric Crystals* (Rostov University Press, Rostov-on-Don, 1990).

[46] G. Hayward, J. Bennett, and R. Hamilton, A theoretical study on the influence of some constituent material properties on the behaviour of 1–3 connectivity composite transducers, J. Acoust. Soc. Am. **98**, 2187 (1995).

[47] E. Sun and W. Cao, Relaxor-based ferroelectric single crystals: Growth, domain engineering, characterization and applications, Prog. Mater. Sci. **65**, 124 (2014).

[48] A. Kozioł-Rachwał, W. Skowroński, T. Ślęzak, D. Wilgocka-Ślęzak, J. Przewoźnik, T. Stobiecki, Q. H. Qin, S. van Dijken, and J. Korecki, Room-temperature perpendicular magnetic anisotropy of MgO/Fe/MgO ultrathin films, J. Appl. Phys. **114**, 224307 (2013).

[49] R. C. Hall, Magnetic anisotropy and magnetostriction of ordered and disordered cobalt-iron alloys, J. Appl. Phys. **31**, S157 (1960).

[50] I. S. Jacobs, Magnetic properties in the system iron-cobalt-aluminum, IEEE Trans. Magn. **MAG-21**, 1306 (1985).

[51] G. Bayreuther, M. Dumm, B. Uhl, R. Meier, and W. Kipferl, Magnetocrystalline volume and interface anisotropies in epitaxial films: Universal relation and Néel's model, J. Appl. Phys. **93**, 8230 (2003).

[52] S. Ikeda, K. Miura, H. Yamamoto, K. Mizunuma, H. D. Gan, M. Endo, S. Kanai, J. Hayakawa, F. Matsukura, and H. Ohno, A perpendicular-anisotropy CoFeB–MgO magnetic tunnel junction, Nat. Mater. **9**, 721 (2010).

[53] S. Zhang, Y. G. Zhao, P. S. Li, J. J. Yang, S. Rizwan, J. X. Zhang, J. Seidel, T. L. Qu, Y. J. Yang, Z. L. Luo, Q. He, T. Zou, Q. P. Chen, J. W. Wang, L. F. Yang, Y. Sun, Y. Z. Wu, X. Xiao, X. F. Jin, J. Huang, C. Gao, X. F. Han, and R. Ramesh, Electric-Field Control of Nonvolatile Magnetization in Co$_{40}$Fe$_{40}$B$_{20}$/Pb(Mg$_{1/3}$Nb$_{2/3}$)$_{0.7}$Ti$_{0.3}$O$_3$ Structure at Room Temperature, Phys. Rev. Lett. **108**, 137203 (2012).

[54] S.-E. Park and T. R. Shrout, Ultrahigh strain and piezoelectric behavior in relaxor based ferroelectric single crystals, J. Appl. Phys. **82**, 1804 (1997).

[55] T. Nan, Z. Zhou, M. Liu, X. Yang, Y. Gao, B. A. Assaf, H. Lin, S. Velu, X. Wang, H. Luo, J. Chen, S. Akhtar, E. Hu, R. Rajiv, K. Krishnan, S. Sreedhar, D. Heiman, B. M. Howe, G. J. Brown, and N. X. Sun, Quantification of strain and charge co-mediated magnetoelectric coupling on

ultra-thin Permalloy/PMN-PT interface, Sci. Rep. **4**, 3688 (2014).

[56] C.-G. Duan, J. P. Velev, R. F. Sabirianov, W. N. Mei, S. S. Jaswal, and E. Y. Tsymbal, Tailoring magnetic anisotropy at the ferromagnetic/ferroelectric interface, Appl. Phys. Lett. **92**, 122905 (2008).

[57] G. Srinivasan, A. S. Tatarenko, and M. Bichurin, Electrically tunable microwave filters based on ferromagnetic resonance in ferrite-ferroelectric bilayers, Electron. Lett **41**, 596 (2005).

[58] Y. K. Fetisov and G. Srinivasan, Electric field tuning characteristics of a ferrite-piezoelectric microwave resonator, Appl. Phys. Lett. **88**, 143503 (2006).

[59] A. S. Tatarenko, G. Srinivasan, and M. I. Bichurin, Magnetoelectric microwave phase shifter, Appl. Phys. Lett. **88**, 183507 (2006).

[60] T. Wu and G. P. Carman, Ultra-low power electrically reconfigurable magnetoelectric microwave devices, J. Appl. Phys. **112**, 073915 (2012).